PAPER

Check for updates

g-C₃N₄ promoted MOF derived hollow carbon nanopolyhedra doped with high density/fraction of single Fe atoms as an ultra-high performance non-precious catalyst towards acidic ORR and PEM fuel cells†

Yijie Deng,‡[ab] Bin Chi,‡[a] Xinlong Tian, [ID][a] Zhiming Cui,[a] Ershuai Liu,[d] Qingying Jia,[d] Wenjun Fan,[a] Guanghua Wang,[a] Dai Dang, [ID][a] Minsi Li,[c] Ketao Zang,[e] Jun Luo,[e] Yongfeng Hu,[f] Shijun Liao, [ID] *[a] Xueliang Sun [ID] *[c] and Sanjeev Mukerjee[d]

We report a hollow carbon nanopolyhedron catalyst doped with N and single Fe atoms, prepared by pyrolyzing hollow ZIF-8 with ferric acetylacetonate and g-C₃N₄. The catalyst retains the polyhedral morphology of its precursor and possesses exclusively Fe–N₄ moieties promoted by g-C₃N₄ nitriding, evidenced by multipronged microscopic and spectroscopic analyses. In rotating disk measurements, the catalyst exhibits superior ORR activity in both acidic and alkaline media, with a half-wave potential of 0.78 V in the former and 0.845 V in the latter. In addition, its ORR stability surpasses that of commercial Pt/C in acidic and alkaline media. Most notably, the catalyst exhibits ultra-high performance in a H_2/O_2 proton exchange membrane fuel cell (PEMFC), with a current density of 400 mA cm⁻² at 0.7 V and 133 mA cm⁻² at 0.8 V, and a maximum power density of 628 mW cm⁻². This is among the best PEMFC performances reported for cathodes free of platinum-group metals. We attribute this excellent-ORR activity to the integration of the high density Fe(II)–N₄–H₂O moiety (4.51956 × 10¹³ sites cm⁻²) embedded in the carbon framework, identified by *in situ* X-ray absorption spectroscopy, and the well-balanced micro/meso/macroporous structure.

1. Introduction

Proton exchange membrane fuel cells (PEMFCs) are one of the most promising alternative power sources and energy storage technologies due to their high energy-conversion efficiency, environmental safety, and other outstanding features. However, widespread utilization and large-scale commercialization of

[a]*The Key Laboratory of Fuel Cell Technology of Guangdong Province, School of Chemistry and Chemical Engineering, South China University of Technology, Guangzhou 510641, China. E-mail: chsjliao@scut.edu.cn*

[b]*School of Environment and Civil Engineering, Dongguan University of Technology, Dongguan, China*

[c]*Department of Mechanical and Materials Engineering, University of Western Ontario, 1151 Richmond St., London, Ontario, Canada N6A 3K7. E-mail: xsun9@uwo.ca*

[d]*Department of Chemistry and Chemical Biology, Northeastern University, Boston, Massachusetts, 02115, USA*

[e]*Center for Electron Microscopy, TUT-FEI Joint Laboratory, Tianjin Key Laboratory of Advanced Functional Porous Materials, Institute for New Energy Materials & Low-Carbon Technologies, School of Materials Science and Engineering, Tianjin University of Technology, Tianjin 300384, China*

[f]*Canadian Light Source, 44 Innovation Boulevard, Saskatoon, SK, Canada S7N 2V3*

† Electronic supplementary information (ESI) available. See DOI: 10.1039/c8ta11785c

‡ Deng and Chi contributed equally to this work.

PEMFCs have been severely hindered by the sluggish kinetics of the oxygen reduction reaction (ORR) at the cathode, which currently demands large amounts of scarce, expensive Pt.[1–3]

As one of the most promising alternatives to Pt-based catalysts, carbon systems co-doped with transition metal and nitrogen (M–N$_x$/C, M = Fe, Co, *etc.*) have attracted major attention because of their excellent ORR performance and the abundance of their constituents.[4,5] It is widely believed that the high inherent activity (*i.e.*, turnover frequency) of active sites in Fe–N$_x$/C catalysts originates primarily from nitrogen-coordinated single Fe atoms embedded in the carbon matrix with nearly optimized oxygen adsorption energy.[6] In addition, the high surface area and favorable porous structure of M–N$_x$/C promote ORR performance by exposing an abundance of active sites.[7–9]

In recent years, considerable effort has been channeled into constructing high-density Fe–N$_x$ sites by making Fe highly dispersed at the atomic level and by optimizing the composition and electronic structure of the carbon matrix, such as the basicity.[10–17] Most Fe–N$_x$/C electrocatalysts are synthesized *via* the high-temperature pyrolysis of precursors containing Fe, N, and C.[7,18] In some processes, samples are annealed under a toxic NH₃ atmosphere to achieve high-density atomic Fe–N$_x$ sites by boosting the N content.[19,20] However, in many cases, most of the

Fe and N exist in the catalyst as uncontrollable agglomerations embedded in the carbon skeleton rather than as active Fe–N$_x$ structures.[21,22] In addition, it is usually difficult to obtain a suitable porous structure, as the morphologies of precursors are often destroyed by high-temperature treatments.[18,23,24] It is therefore desirable to develop an efficient strategy for realizing a highly efficient doped carbon catalyst containing both a high density of atomic Fe–N$_x$ sites and an optimal porous structure.[25,26]

Zeolite imidazolate frameworks (ZIFs) have emerged as ideal precursors for the preparation of N-doped carbon materials because they have a well-defined morphology/structure, a high surface area, and abundant N-containing ligands.[15,27,28] Much effort has been devoted to developing ORR catalysts derived from metal–organic frameworks (MOFs) with high active-site densities, distinctive morphologies, and porous structures.[29,30] For instance, Wu et al.[31] reported a ZIF-derived catalyst doped with N-coordinated single Co atoms that when used as the cathode catalyst in a H$_2$/O$_2$ fuel cell achieved a power density of 0.56 W cm^{-2}. Jiang et al.[32] used a porphyrinic MOF as the precursor to prepare N-doped porous carbon implanted with single-atom Fe via a mixed-ligand strategy; the catalyst yielded a half-wave potential of 0.776 V towards the ORR in an acidic medium. Recent reports have also indicated that a hollow structure appears to enhance a catalyst's ORR performance.[28,33–35] Yet while excellent progress has been made, it is still a grand challenge (1) to investigate the origin of high ORR activity of single-atom catalysts (SACs) and the coordination environment of single-atom during the oxygen reduction reaction; (2) to obtain a high-performance ORR catalyst with high PEMFC performance; and (3) to improve the performance of Fe-doped carbon catalysts by tuning their morphology/structure and increasing their active-site density through the atomic dispersion of doped Fe and the formation of high-density Fe–N$_4$ active structures (with single metal loadings >1 wt%).[32]

In this work, we designed and prepared hollow carbon polyhedra co-doped with single Fe atoms and N, using tannic acid as the etching agent to obtain a hollow ZIF-8 precursor. Ferric acetylacetonate was employed as the Fe precursor to realize the atomic-scale dispersion of Fe, and g-C$_3$N$_4$ was further used as a nitriding agent to achieve a high density of Fe–N$_4$ active structures. The catalyst retained the polyhedral morphology of ZIF-8 and the hollow structure of the precursor. The doped Fe was highly dispersed in the material, resulting in a high density of Fe–N$_4$ sites. The catalyst exhibited excellent activity and durability towards the ORR in both acidic and alkaline solutions. Most notably, it yielded outstanding PEMFC performance with our optimal catalyst as the cathode in the MEA, making this one of the best PEMFC performances reported for cathodes free of platinum-group metals.

2.   Experimental procedures

2.1   Electrocatalyst preparation

Synthesis of ZIF-8 and hollow ZIF-8. The ZIF-8 polyhedra were synthesized by a previously reported method with a slight modification, as follows: 4 g 2-methylimidazole was dissolved in 25 mL methanol, then 1 g Zn(NO$_3$)$_2$·6H$_2$O in 10 mL methanol was added to this solution under stirring, and the final mixture was stirred constantly for 24 h at room temperature. The product was obtained by centrifugation, washed with methanol, and vacuum dried.[36] The hollow ZIF-8 was prepared by adding 40 mg of as-prepared ZIF-8 into 3 mL water, after which a tannic acid solution (56 mg of tannic acid, 7 mL water) was added. Ultimately, the concentrations of ZIF-8 and tannic acid were about 4.0 mg mL^{-1} and 5.6 mg mL^{-1}, respectively. After about 15 min, the product was collected by centrifugation, washed with deionized water, and vacuum dried. The obtained product is denoted as HZ8.[37]

Synthesis of g-C$_3$N$_4$. Melamine with a mass of 6.0 g was put into a crucible with a lid and kept in static air in a muffle furnace at 550 °C for 4 h at a rate of 6 °C min^{-1} to obtain g-C$_3$N$_4$.[38–41]

Preparation of catalysts. 40 mg HZ8 was prepared by adding it in 3 mL methanol, after which a ferric acetylacetonate solution (80 mg of ferric acetylacetonate and 4 mL methanol) was added, giving a mass ratio of ferric acetylacetonate/HZ8 of 2. After 6 h to allow for diffusion and dispersion under stirring, the sample was collected by centrifugation, washed with methanol, and vacuum dried.

This FeHZ8 was mixed with g-C$_3$N$_4$, yielding g-C$_3$N$_4$/FeHZ8 in a ratio of 7.35 : 1. After uniform grinding, the mixture was put into a tubular furnace for pyrolysis under an Ar atmosphere as follows: heated from room temperature to 950 °C at a rate of 2 °C min^{-1}, kept at 950 °C for 3 h, then left to cool to room temperature. It was then leached with 0.5 M H$_2$SO$_4$ for 12 h, washed with deionized water, and pyrolyzed again at a high temperature to achieve graphitization.

We denote the prepared catalysts as C-FeHZ8@g-C$_3$N$_4$-X, in which "X" indicates the pyrolysis temperature. The whole preparation process is represented in Scheme 1.

For comparison, C-HZ8@g-C$_3$N$_4$-950 and C-FeHZ8-950 were prepared using similar procedures but without the addition of ferric acetylacetonate or g-C$_3$N$_4$, respectively.

2.2   Materials characterization

The materials were characterized using a Merlin field emission scanning electron microscope (SEM; Carl Zeiss), a JEM-2100 transmission electron microscope (TEM; JEOL, Japan) operating at 120 kV, a TD-3500 powder diffractometer (Tongda,
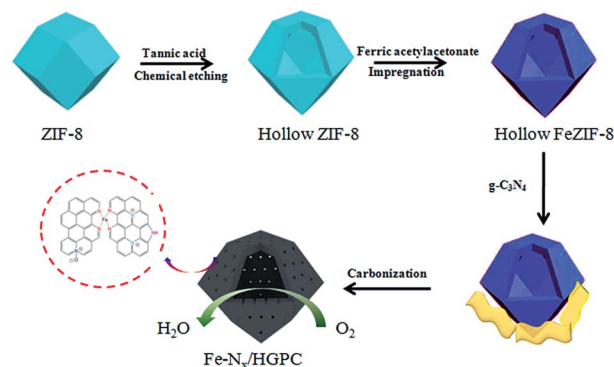
Scheme 1 Schematic illustration of the C-FeHZ8@g-C$_3$N$_4$-950 synthesis.

China) operating at 30 kV and 20 mA, using Cu-Kα radiation sources, X-ray photoelectron spectroscopy (VG ESCALAB MK2 X-ray photoelectron spectrometer, VG Corporation, UK) using an Al-Kα X-ray source, and BET surface area and pore distribution measured on a Tristar 3020 gas adsorption analyzer (Micromeritics, USA) at 77 K. In addition, Mössbauer spectra were recorded at room temperature with a Topologic 500A spectrometer using a $^{57}Co(Rh)$ source moving in a constant acceleration model (MFD-500AV, Japan). X-ray absorption spectroscopy (XAS) measurements were conducted on the beamline 8-ID at the National Synchrotron Light Source II (NSLS-II), Brookhaven National Laboratory. An electrode composed of dry powders was measured ex situ at the Fe K-edge. Then the dry electrode was immersed in 0.1 M $HClO_4$ under a weak vacuum to remove surface oxides, trapped gas, and other unwanted materials. In situ XAS values were collected at the Fe K-edge as a function of applied potentials in O_2-purged 0.1 M $HClO_4$, following our regular testing protocol.[42]

2.3 Electrocatalytic testing

All electrochemical measurements were conducted using an Ivium electrochemical workstation (Ivium, Netherlands) in a standard three-electrode system, with a Ag/AgCl reference electrode for the acidic medium and a Hg/HgO reference electrode for the alkaline medium. A Pt wire was used as the counter electrode and a glassy carbon (GC) electrode as the working electrode substrate (0.196 cm^2). All carbon catalyst-loaded electrodes were prepared by the following procedure: 5 mg catalyst was ultrasonically dispersed in 1 mL Nafion/ethanol solution (0.25 wt% Nafion), yielding a catalyst ink. Then 20 μL of the catalyst ink was pipetted onto a GC substrate electrode and dried under infrared radiation. The catalyst loading was about 0.5 mg cm^{-2}.

Linear scanning voltammetry (LSV) and cyclic voltammetry (CV) were conducted at a scan rate of 10 mV s^{-1} in O_2- or N_2-saturated 0.1 M KOH electrolyte or 0.1 M $HClO_4$ electrolyte.

The electron transfer numbers (n) per oxygen molecule during oxygen reduction were calculated with the Koutecky–Levich (K–L) equation:

$$J^{-1} = J_k^{-1} + (0.62nFCD^{2/3}\gamma^{-1/6}\omega^{1/2})^{-1}$$

where J is the measured current density, J_k is the kinetic current density, n is the electron transfer number, ω is the electrode rotation rate, F is the Faraday constant, C is the O_2 saturation concentration in the electrolyte, D is the O_2 diffusion coefficient in the electrolyte, and γ is the kinetic viscosity of the electrolyte.

In this work, chronoamperometry was applied to evaluate the catalysts' durability. It was conducted at 0.65 V for 24 h at a rotation rate of 900 rpm in an O_2-saturated 0.1 M KOH solution, and at 0.62 V for 24 h at a rotation rate of 900 rpm in an O_2-saturated 0.1 M $HClO_4$ solution.

2.4 Single PEM fuel cell measurement

Membrane electrode assemblies (MEAs) with our doped carbon catalysts as the cathode were prepared using a catalyst-sprayed

membrane method reported previously by our group.[25,43] The typical preparation was as follows. First, the catalyst ink was prepared by mixing the catalyst, Nafion solution, and isopropyl alcohol, followed by ultrasonication. Next, the ink was sprayed on one side of a pretreated Nafion 211 membrane (DuPont, USA) to form the cathode catalyst layer. The anode catalyst layer was prepared by the same procedure but using a commercial Pt/C catalyst. The active area of the MEA was 5.0 cm^2. The catalyst loading in the cathode was 4 mg cm^{-2}, and the Pt loading in the anode was 0.1 mg cm^{-2}.

Performance measurements of the MEAs were conducted in a H_2/O_2 single cell with an Arbin fuel cell testing system (Arbin, USA). The fuel and oxidant were fully humidified at 30 psi back pressure, and both had a flow rate of 300 mL min^{-1}. The cell temperature was 80 °C.

3. Results and discussion

We took SEM and TEM images of the samples with and without the C_3N_4 and/or Fe precursors to investigate their roles in the products' morphologies and ORR activities (Fig. 1). All three samples retained the morphology of the ZIF-8 precursor (Fig. 1a–c), exhibiting a polyhedral shape and hollow structure, as revealed by TEM (Fig. 1d–f). The particle size of the final catalyst was slightly smaller than that of the precursor because the organic carbon skeleton contracts during the high-temperature treatment (Fig. S1†).[44] Amazingly, many inorganic Fe species were clearly present in the sample without the C_3N_4 precursor (Fig. 1f) but not in the one with it (Fig. 1e). This obviously suggests that C_3N_4 prevented Fe-agglomeration during the high temperature treatment and preferentially promoted the formation of Fe–N_4 moieties.[45,46]

The HAADF-STEM image displayed in Fig. 2a reveals the hollow polyhedral shape of C-FeHZ8@g-C_3N_4-950, and the elemental maps (Fig. 2b) show the homogeneous distribution of Fe and N in the hollow carbon framework. This is further evidenced by the high-resolution STEM images (Fig. 2c and d), which capture the presence of abundant and dispersed single atoms in the carbon framework. The high density of Fe in the sample shown in Fig. 2c can be ascribed to our preparation process, which promoted the entrance of the Fe precursor into the internal channels of ZIF-8, and g-C_3N_4 also facilitated the formation of the Fe–N_4 coordination structure during pyrolysis.

Fig. 3a and b present the XRD patterns of all the samples before and after acid leaching, respectively. No peaks associated with inorganic Fe species (such as oxides, carbides, nitrides, etc.) are observable for the C-FeHZ8@g-C_3N_4-950 sample either before or after acid leaching, corroborating the TEM results. In contrast, some weak peaks arising from iron oxides and iron carbides are discernable in the XRD patterns of C-FeHZ8-950 (which contained no g-C_3N_4 in the precursor), even after acid leaching. It is noteworthy that compared to some other reported single-atom Fe-doped carbon catalysts,[46] C-FeHZ8@g-C_3N_4-950 before acid leaching showed no peaks associated with iron oxides, Fe, or iron carbides. These results suggest that our preparation approach using ferric acetylacetonate suppressed the formation of iron oxide and carbide (unlike when ferric
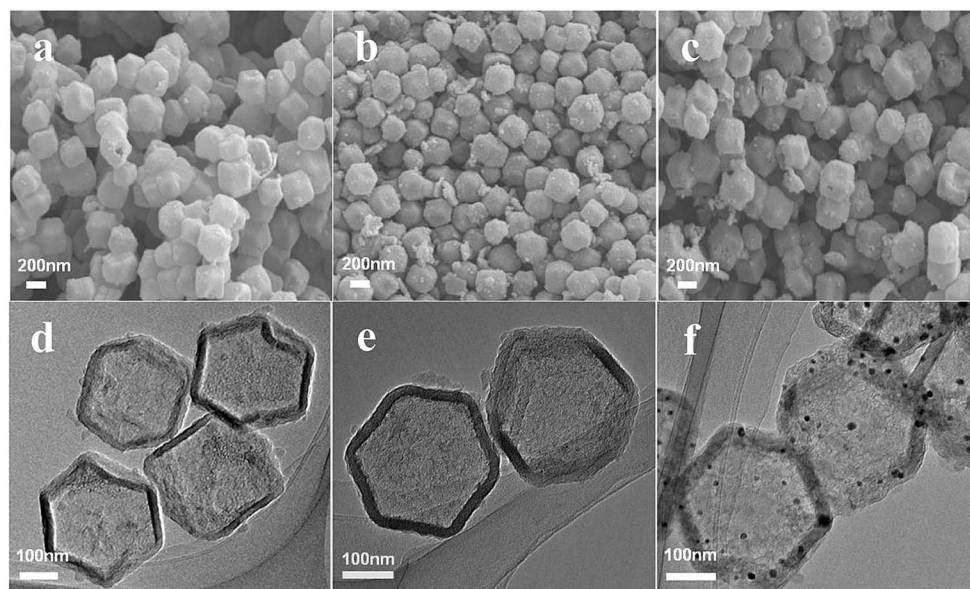
Fig. 1 SEM images of (a) C-HZ8-950, (b) C-FeHZ8@g-C$_3$N$_4$-950, and (c) C-FeHZ8-950; TEM images of (d) C-HZ8-950, (e) C-FeHZ8@g-C$_3$N$_4$-950, and (f) C-FeHZ8-950.

inorganic salts are used as the Fe precursor[46]), and that the formation of iron oxide and carbide is entirely prevented by adding g-C$_3$N$_4$. g-C$_3$N$_4$ decomposed into nitrogenous and carbonaceous gases (*e.g.*, C$_2$N$_2$+, C$_3$N$_2$+, and C$_3$N$_3$+) at 950 °C, and these cyano fragments may have reacted with Fe to make

Fe–N$_x$ structures *via* nitrogen-doping reactions, resulting in the exclusive formation of the Fe–N$_x$ moieties.

The Raman spectra of samples C-FeHZ8@g-C$_3$N$_4$-950 and C-FeHZ8-950 exhibited two prominent peaks (Fig. 3c). The *D* band is related to the local defects and the disordered sp^2-hybridized carbon induced by carbon heteroatoms,[47–50] whereas the G band
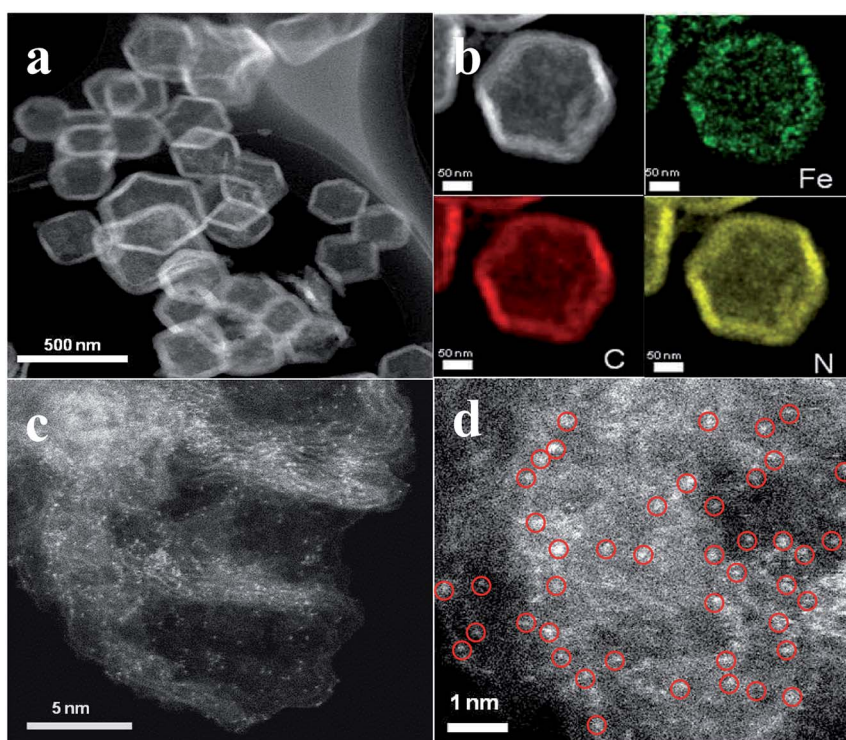

Fig. 2 HAADF-STEM image (a), elemental mapping image (b), AC HAADF-STEM image with high resolution (c), and enlargement of image (d) in (c) of C-FeHZ8@g-C$_3$N$_4$-950.
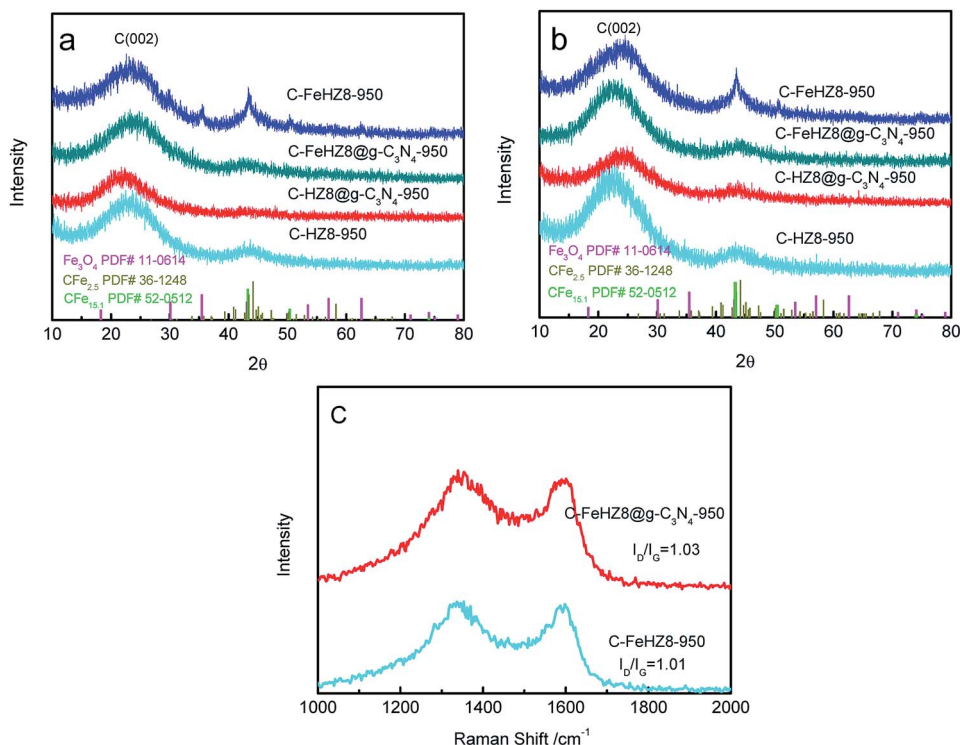
This journal is © The Royal Society of Chemistry 2019

J. Mater. Chem. A, 2019, **7**, 5020–5030 | **5023**

Fig. 3 XRD patterns of C-HZ8-950, C-HZ8@g-C_3N_4-950, C-FeHZ8-950, and C-FeHZ8@g-C_3N_4-950 (a) before acid leaching and (b) after acid leaching; (c) Raman spectra of C-FeHZ8-950 and C-FeHZ8@g-C_3N_4-950.

is associated with the tangential stretching mode of sp^2 carbon atoms, indicating the existence of crystalline graphitic carbon in the carbon material.[51] The I_D/I_G ratios of C-FeHZ8@g-C_3N_4-950 and C-FeHZ8-950 were 1.03 and 1.01 respectively, revealing that C-FeHZ8@g-C_3N_4-950 may have possessed more abundant defect sites that favored a host of pyridinic nitrogen,[52] which further suggests that introducing C_3N_4 as a nitriding agent can increase defect sites in the carbon skeleton.[49]

N_2 adsorption–desorption isotherms and the corresponding pore-size distribution curves of all the samples are shown in Fig. S5.† For C-FeHZ8@g-C_3N_4-950, a typical Type IV isotherm with hysteresis loops in the medium- and high-pressure regions ($P/P_o = 0.5–1.0$) is observable, indicating that a meso/macroporous structure dominates this sample, along with copious micropores;[53,54] the BET area reached up to 754 m^2 g^{-1}. The well-balanced micro/meso/macropores in C-FeHZ8@g-C_3N_4-950 may be attributed to the gas etching that occurred during the thermal decomposition of g-C_3N_4.

Fig. S6† shows the CV curves of sample C-FeHZ8@g-C_3N_4-950 in a nitrogen- or oxygen-saturated 0.1 M $HClO_4$ or 0.1 M KOH electrolyte. In a nitrogen atmosphere, no redox peaks are observable in the CV curves, but it exhibited a well-defined oxygen reduction peak in both O_2-saturated 0.1 M KOH (Fig. S6a†) and 0.1 M $HClO_4$ (Fig. S6b†) solutions.

The superior ORR activity of C-FeHZ8@g-C_3N_4-950 in both acidic and alkaline media is further confirmed by the LSV curves displayed in Fig. 4a and b. The ORR activities followed the order C-HZ8-950 < C-HZ8@g-C_3N_4-950 < C-FeHZ8-950 < C-FeHZ8@g-C_3N_4-950 in both 0.1 M $HClO_4$ and 0.1 M KOH

solutions (Fig. 4b and a). This activity trend makes sense if the Fe–N_x moieties are responsible for the high ORR activity; Fe doping initiates the formation of Fe–N_x moieties, which are further selectively promoted by the addition of g-C_3N_4 to the precursor. With our optimal C-FeHZ8@g-C_3N_4-950 catalyst, the half-wave potential was superior to that of the commercial Pt/C catalyst: 30 mV in an alkaline medium, and only 60 mV lower than that of commercial Pt/C in an acidic medium (0.78 V *vs.* 0.84 V), which is comparable to the performance of state-of-the-art Fe–N–C (see Tables S1 and S2†). Koutecky–Levich analysis (Fig. 4c and d) indicates that the electron transfer numbers (n) for C-FeHZ8@g-C_3N_4-950 in alkaline and acidic electrolytes are 3.96 and 3.70, respectively, suggesting that C-FeHZ8@g-C_3N_4-950 followed a predominantly four-electron ORR pathway in both electrolytes. We normalized the ORR activities of four samples in acid and alkaline media to their physical surface area and mass, and compared the results in Fig. S9,†[55] clearly, C-FeHZ8@g-C_3N_4-950 exhibited the highest ORR activities (both mass activity and specific activity) in both acid and alkaline media, especially in acid mediums, the mass activity and specific activity of C-FeHZ8@g-C_3N_4-950 are 2.88 times and 3.09 times higher than C-FeHZ8@-950 without g-C_3N_4 addition, and 13.1 times and 16.42 times higher than C-HZ8@g-C_3N_4-950 without addition of Fe, respectively.

In addition, C-FeHZ8@g-C_3N_4-950 exhibited excellent stability in both electrolytes (Fig. 4e and f), evaluated *via* elongated chronoamperometric measurement. In 0.1 M KOH solution, the current density of commercial Pt/C decreased by 11%, whereas C-FeHZ8@g-C_3N_4-950 lost only 4% of its initial ORR
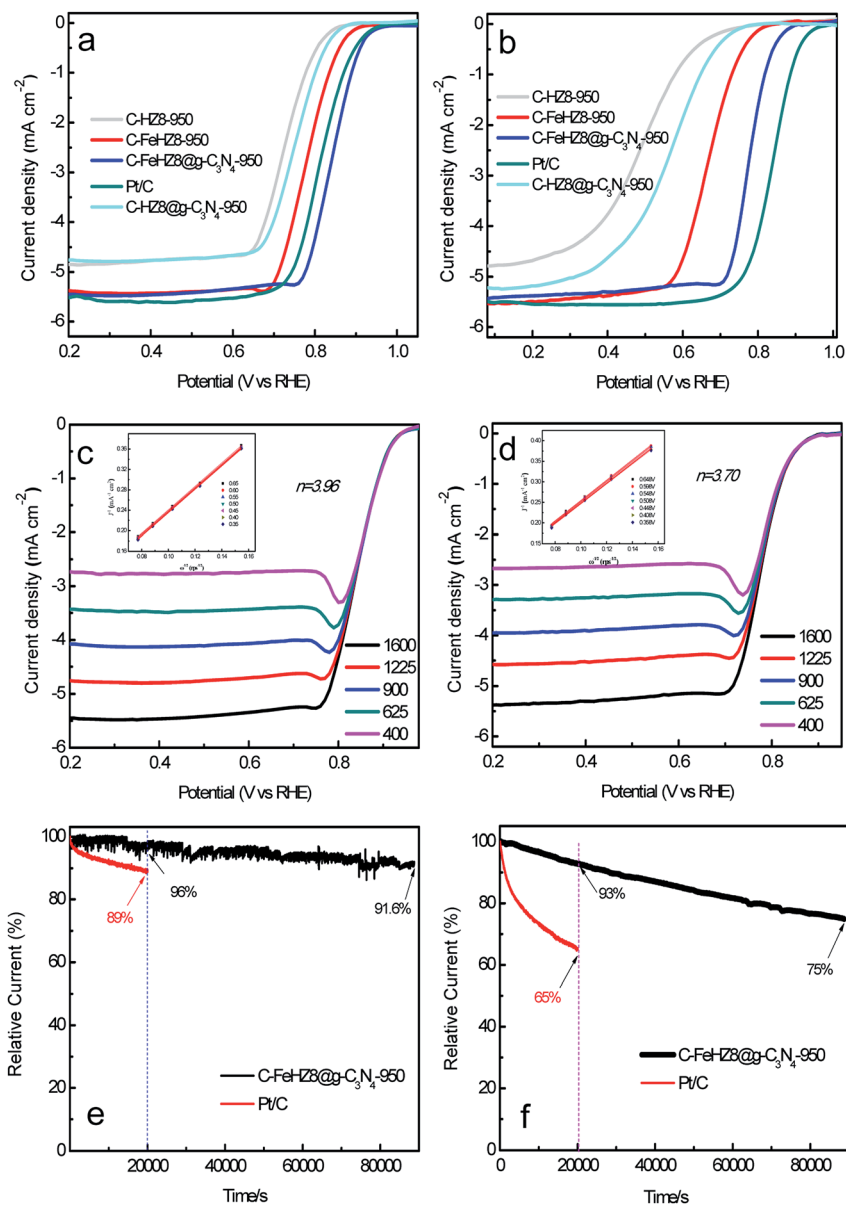
Fig. 4 LSV curves of C-HZ8-950, C-HZ8@g-C$_3$N$_4$-950, C-FeHZ8-950, C-FeHZ8@g-C$_3$N$_4$-950, and 20 wt% Pt/C in (a) O$_2$-saturated 0.1 M KOH and (b) 0.1 M HClO$_4$ (rotation rate: 1600 rpm); (c) ORR curves of C-FeHZ8@g-C$_3$N$_4$-950 obtained at different rotation rates (from 400 to 1600 rpm) in (c) O$_2$-saturated 0.1 M KOH and (d) 0.1 M HClO$_4$. The insets in (c) and (d) show K–L plots of J^{-1} *versus* $\omega^{-1/2}$ and electron transfer number. Durability testing results of C-FeHZ8@g-C$_3$N$_4$-950 and Pt/C in (e) O$_2$-saturated 0.1 M KOH and (f) 0.1 M HClO$_4$.

performance (for 5.55 h), and still retained 91.6% of its initial ORR performance for 24 h testing. In 0.1 M HClO$_4$ solution, C-FeHZ8@g-C$_3$N$_4$-950 retained more than 93% of its original current density, whereas commercial Pt/C exhibited a current loss of 35% for 5.55 h. Continuing to test for 24 h, C-FeHZ8@g-C$_3$N$_4$-950 retained 75% of its initial ORR performance.

Encouraged by the excellent ORR performance of C-FeHZ8@g-C$_3$N$_4$-950 and C-FeHZ8-950 evaluated in rotating disk electrodes (RDEs), we investigated their performance as the cathode catalysts in H$_2$/O$_2$ PEMFCs (Fig. 5). The optimal cathode performance of C-FeHZ8@g-C$_3$N$_4$-950 was obtained with a catalyst loading of 4 mg cm^{-2} (see Fig. S10†): current densities were 400 mA cm^{-2} at 0.7 V and 133 mA cm^{-2} at 0.8 V,

and the maximum power density reached up to 628 mW cm^{-2}. It indicates that C-FeHZ8@g-C$_3$N$_4$-950 is among the rank of excellent doped carbon catalysts in the H$_2$/O$_2$ PEMFCs (Table S3†). It is notable that the maximum power density of C-FeHZ8-950 was only 239 mW cm^{-2}, 38% of that of C-FeHZ8@g-C$_3$N$_4$-950. This dramatic performance difference highlights the critical role of g-C$_3$N$_4$ in promoting the selective formation of Fe–N$_x$ moieties. Furthermore, we also investigated the durability of our catalyst in a single PEMFC; the current density loss at 0.7 V was 51.3% after 8 h testing (Fig. S11†), which is actually little better than those reported previously for Fe–N$_x$/C electrocatalysts.[56–58] To investigate the possible causes of decay, we measured the dissolution of iron active species by the ICP-AES
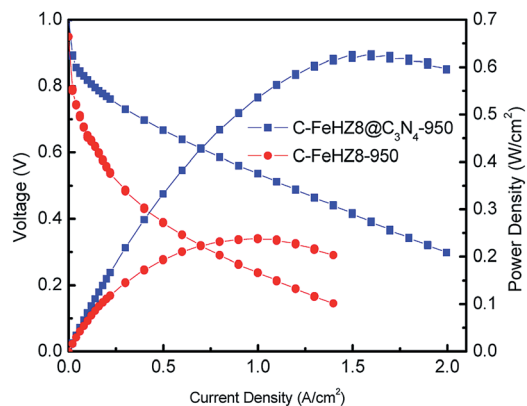
Fig. 5 Polarization curves and power-density plots for a H_2/O_2 PEMFC: comparing results with C-FeHZ8@g-C$_3$N$_4$-950 or C-FeHZ8-950 as the cathode catalyst.

analysis, it was found that the dissolution of Fe is up to 21.7 wt% after dispersing the C-FeHZ8@g-C$_3$N$_4$-950 sample in 0.1 M HClO$_4$ solution for 24 h. Clearly, the dissolution of iron active species may be one of the important reasons resulting in the decay of catalyst performance. In addition, water flooding and the Fenton reaction may also be the reasons for the decay.

To investigate the beneficial roles of g-C$_3$N$_4$ and the surface chemical states of the catalysts, X-ray photoelectron spectroscopic (XPS) analysis was conducted on C-FeHZ8-950 and C-FeHZ8@g-C$_3$N$_4$-950 (Fig. 6). The N content of C-FeHZ8@g-C$_3$N$_4$-950 was up to 6.57 at%, almost three times that of C-FeHZ8-950

(2.42 at%), demonstrating the significance of g-C$_3$N$_4$ for enriching the N content, and contained a high loading of Fe (up to 3.17 wt%). Moreover, g-C$_3$N$_4$ seemed to greatly suppress the formation of oxidized N and promote the formation of pyridinic nitrogen (Fig. 6c and d); the pyridinic-N fraction increased from 17.27 at% with C-FeHZ8-950 to 41.9 at% with C-FeHZ8@g-C$_3$N$_4$-950. In addition, the oxidized N content decreased from 35.8 at% with C-FeHZ8-950 to 7.0 at% with C-FeHZ8@g-C$_3$N$_4$-950. It has been recognized that the nitrogen in Fe–N$_x$ moieties formed through high-temperature pyrolysis is pyridinic N.[59,60] Thus, the g-C$_3$N$_4$-induced enrichment of pyridinic N promotes the formation of Fe–N$_x$ moieties, thereby enhancing the ORR. Furthermore, pyridinic-N could promote to catalyze the ORR by providing active sites.[51]

The fractions of the Fe–N$_x$ moieties in C-FeHZ8@g-C$_3$N$_4$-950 and C-FeHZ8-950 were 11.34 and 6.85 at%, respectively. Given the N contents in these samples (6.57 and 2.42 at%), the calculated contents of N bonded with Fe were 0.745 at% and 0.166 at%, respectively. In other words, the density of the Fe–N$_x$ moieties in C-FeHZ8@g-C$_3$N$_4$-950 was 4.5 times the density in C-FeHZ8-950, which may be a reasonable explanation for the superior ORR performance of C-FeHZ8@g-C$_3$N$_4$-950.

As shown in Fig. 7, the C-FeHZ8@g-C$_3$N$_4$-950 and C-FeHZ8-950 samples exhibited markedly different ^{57}Fe Mössbauer spectra, which were deconvoluted into the three doublets plus inorganic Fe species listed in Table 1. The three doublets—low-spin site (D1), mid-spin site (D2), and high-spin (D3) site—can be ascribed to Fe(ɪɪ) coordinated with N ligands with different spin states. The D3 moiety is believed to have the highest
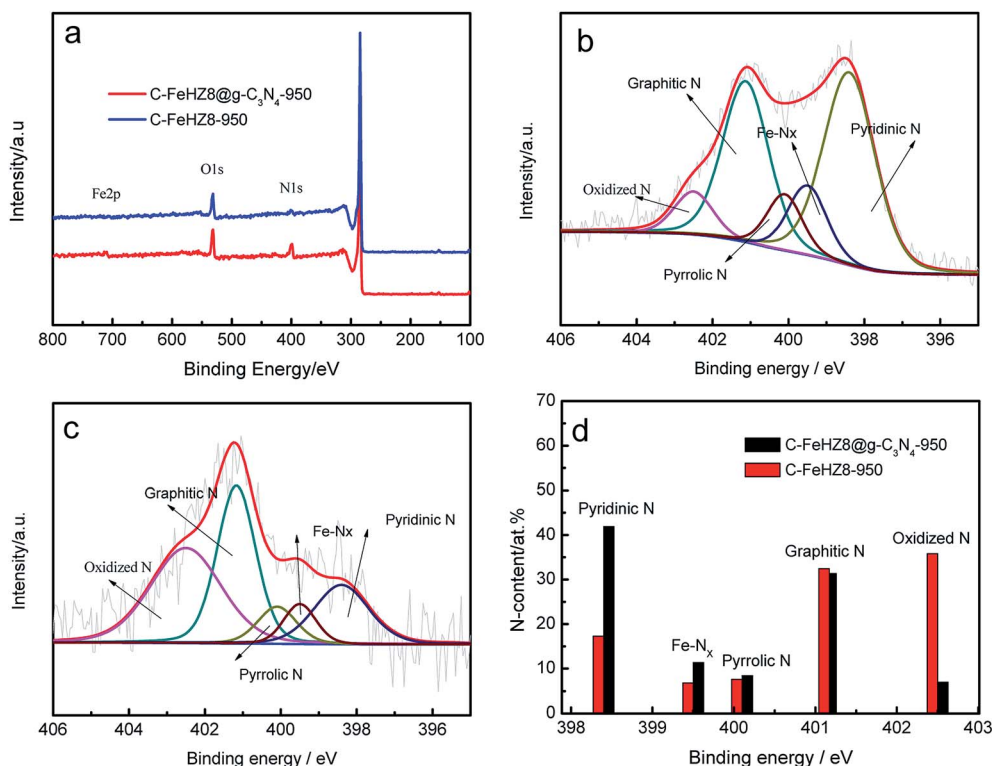

Fig. 6 (a) Survey XPS spectra and (b) high-resolution N1s XPS spectra of C-FeHZ8@g-C$_3$N$_4$-950; (c) high-resolution N1s XPS spectra of C-FeHZ8-950; (d) fractions of the different N species present in C-FeHZ8-950 and C-FeHZ8@g-C$_3$N$_4$-950.

5026 | *J. Mater. Chem. A*, 2019, **7**, 5020–5030

This journal is © The Royal Society of Chemistry 2019

intrinsic ORR activity among the three.[61] With the addition of g-C_3N_4, the relative contents (relative absorption areas) of the D1, D2, and D3 moieties in C-FeHZ8@g-C_3N_4-950 were far higher than that of C-FeHZ8-950 without g-C_3N_4, further confirming the g-C_3N_4-induced selective formation of Fe–N_4 moieties.

Another key difference between the ^{57}Fe Mössbauer spectra of C-FeHZ8-950 and C-FeHZ8@g-C_3N_4-950 is that the former contained up to 37.61% and 25.26% singlet and sextet moieties, respectively, whereas the latter did not. According to the literature, the singlet can be assigned to incomplete Fe–N_4-like sites that quickly dissolve when in contact with an acid,[10] and the sextet can be assigned to iron oxide.[19] These two moieties are generally inactive towards the ORR in an acidic medium.[62–64] This comparison thus suggests that the addition of g-C_3N_4 promoted the formation of Fe–N_x moieties and suppressed the formation of inorganic Fe species.

To further investigate the Fe electronic and coordination properties of C-FeHZ8@g-C_3N_4-950, *ex situ* and *in situ* X-ray absorption near edge structure (XANES) and extended X-ray absorption fine structure (EXAFS) spectra were collected at the Fe K-edge in an O_2-purged 0.1 M $HClO_4$ electrolyte as a function of applied potentials. As shown in Fig. 8B, the pronounced peak for Fe–N at around 1.47 Å was distinctly observed in C-FeHZ8@g-C_3N_4-950 and iron phthalocyanine (FePc), which was attributed to the presence of Fe–N_x coordination. However, from the Fig. S8b,† *ex situ* Fourier transforms of sample C-FeHZ8-950 showed a distinct peak at about 2.1 Å assigned to the Fe–Fe bond, suggesting that a large number of crystalline iron species with low ORR activity existed in the sample. It also

demonstrates that g-C_3N_4 played a vital in suppressing the formation of less active crystalline iron species and promoting the formation of a high-density Fe–N_x coordination structure. Furthermore, we calculated densities of Fe–N_x sites and active N sites, and they reached up to 4.51956×10^{13} and 3.83906×10^{14} sites cm^{-2}, respectively, based on the results of XPS, ^{57}Fe Mössbauer spectra, BET and XAS analysis. Besides, with increasing potential, the XANES spectra shifted positively to a higher energy (Fig. 8A). At low potentials, the FT-EXAFS spectra exhibited double peaks, which gradually evolved into one prominent peak at high potentials. The XANES and FT-EXAFS spectra collected *ex situ* nearly overlapped with those collected at elevated potentials such as 0.9 V. These XAS observations are consistent with previous observations of Fe–N–C catalysts,[20] suggesting Fe^{3+}/Fe^{2+} redox associated with the adsorption/desorption of oxygen species from active sites. However, one unique aspect of the C-FeHZ8@g-C_3N_4-950 catalyst is the two FT-EXAFS peaks at low potentials such as 0.45 V, which cannot be reasonably fitted using an Fe–N_4 cluster model with equivalent Fe–N paths that gives only one prominent FT-EXAFS peak. Alternatively, a reasonably good fit was obtained using the H_2O–Fe–N_4 cluster model, wherein there is axial bonding with a H_2O molecule in addition to the four Fe–N bonds (Fig. 8C). For consistency, the same model was used to fit the spectrum collected at 0.9 V. The fitting results (Table 2) suggest that the Fe–N bond distance decreases with increasing potential, and the coordination number of Fe–O increases from 1.3 ± 0.5 to 1.8 ± 0.9. These trends suggest a moiety of Fe(II)–N_4–H_2O at low potentials, in which the central Fe is located off the
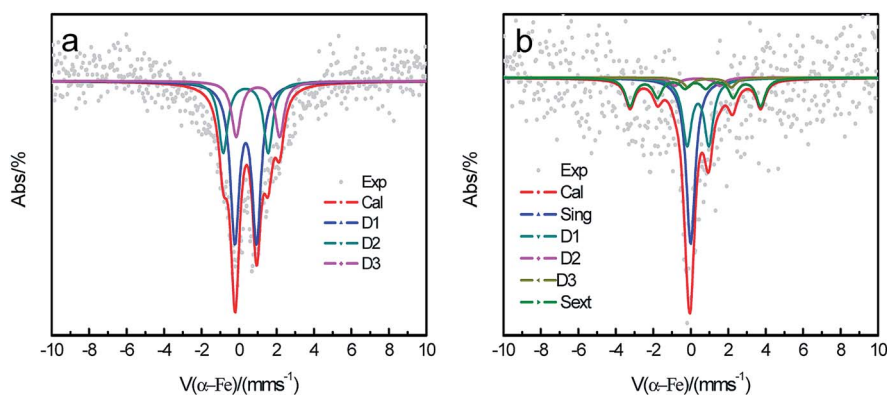

Fig. 7 ^{57}Fe Mössbauer spectroscopy for (a) C-FeHZ8@g-C_3N_4-950 and (b) C-FeHZ8-950.

Table 1 Summary of Mössbauer fitting parameters and the relative absorption peak areas for C-FeHZ8@g-C_3N_4-950 and C-FeHZ8-950

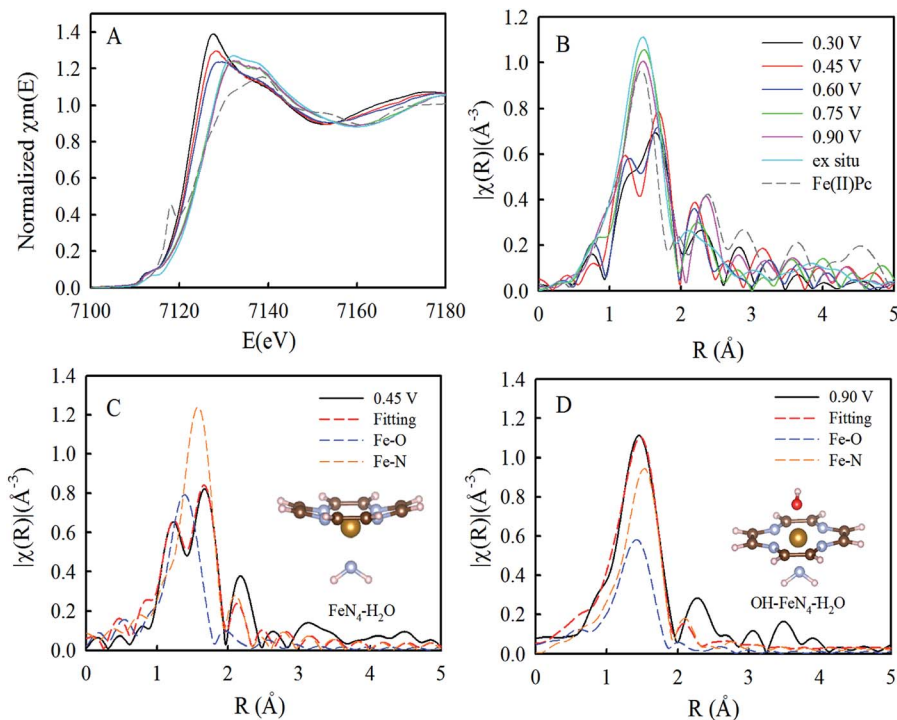| Component	Isomer shift	Q. plotting	Relative absorption area	
			C-FeHZ8@g-C_3N_4-950	C-FeHZ8-950
Singlet	0	—	—	37.61
D1	0.39	1.16	55.01	29.38
D2	0.36	2.40	25.31	3.57
D3	1.01	2.32	19.68	4.19
Sext	0.25	0	—	25.26

This journal is © The Royal Society of Chemistry 2019

J. Mater. Chem. A, 2019, **7**, 5020–5030 | **5027**

Fig. 8 XANES results of iron phthalocyanine (FePc) and C-FeHZ8@g-C$_3$N$_4$-950 (A); Fourier-transformed K-edge EXAFS of Fe for iron phthalocyanine (FePc) and C-FeHZ8@g-C$_3$N$_4$-950 (B); the EXAFS fitting result of C-FeHZ8@g-C$_3$N$_4$-950 at 0.45 V (C), and the EXAFS fitting result of C-FeHZ8@g-C$_3$N$_4$-950 at 0.90 V (D).

plane, as indicated by the long Fe–N bond distance and as expected from the presence of an axial ligand. Note that while H$_2$O was used here as the axial ligand, it could also be other species with N or O atoms. As the potential increases to 0.9 V, the oxidation state of the central Fe switches to +3, and another axial ligand of OH$^-$ from either water activation or O$_2$ cleavage forms and pulls the central Fe back into the plane, as suggested by the increase in the coordination number of Fe–O and the decrease in the bond distance of Fe–N. While this switching behavior has been observed before,[42] the unique observation here is the strong XAS signal indicating the presence of the axial ligand, which is absent from all previously reported Fe–N–C samples. This implies a large amount of the Fe(II)–N$_4$–H$_2$O moiety in the C-FeHZ8@g-C$_3$N$_4$-950 catalyst, which may account for its high ORR activity, since DFT calculations indicate that the axial ligand can significantly boost the turnover frequency of Fe–N$_4$ active sites.[42,65]

Based on the above analyses and discussions, the high performance of the C-FeHZ8@g-C$_3$N$_4$-950 catalyst can be ascribed to: (1) the abundant and uniformly distributed Fe(II)–N$_4$–H$_2$O moieties;[26,47] (2) the catalyst's high surface area and optimal porous carbon, providing a large electrode–electrolyte interface to facilitate catalytic activity; and (3) the catalyst's hollow structure, which may enhance the exposure of Fe–N$_4$ active sites and serve as a buffering reservoir enhancing the mass transfer of oxygen gas and water for H$_2$/O$_2$ PEMFC operation.[34,66]

4. Conclusions

In summary, we developed a high-performance Fe–N$_x$/C catalyst with a well-defined, hollow nanopolyhedral morphology and dominant Fe–N$_x$ moieties. Benefiting from a high density of Fe(II)–N$_4$–H$_2$O active sites, a large surface area, and a hollow, porous structure, the catalyst exhibited superior ORR activity and excellent stability in both alkaline and acidic media in a RDE. In particular, it yielded excellent PEMFC performance. This work may provide a new avenue for the development of high-performance nonprecious-metal electrocatalysts for fuel cells and metal–air batteries.

Table 2 Summaries of the EXAFS fitting results for C-FeHZ8@g-C$_3$N$_4$-950 at 0.45 V and 0.90 V in an O$_2$-saturated 0.1 M HClO$_4$ electrolyte[a]

Potential	$R_{\text{Fe–N}}$ (Å)	$R_{\text{Fe–O}}$ (Å)	$N_{\text{Fe–O}}$	$\sigma^2 \times 10^{-3}$ (Å^2)	E_0
0.45 V	2.09 ± 0.03	1.86 ± 0.03	1.3 ± 0.5	0.005 ± 0.002	2 ± 3
0.90 V	2.05 ± 0.03	1.90 ± 0.06	1.8 ± 0.9	0.005 ± 0.007	0 ± 2

[a] Fits were done separately at the Fe K-edges in R-space, K^2 weighting. 1.0 < R < 2.2 Å and Δk = 2.1–10.3 Å^{-1} were used for fitting. S_0^2 was fixed at 0.787, obtained by fitting iron reference foil. The coordination number of Fe–N was fixed at four for the fitting.

Conflicts of interest

The authors declare no conflict of interest.

Acknowledgements

References

1 M. Shao, Q. Chang, J.-P. Dodelet and R. Chenitz, *Chem. Rev.*, 2016, **116**, 3594–3657.

2 C. Zhu, H. Li, S. Fu, D. Du and Y. Lin, *Chem. Soc. Rev.*, 2016, **45**, 517–531.

3 J. Zhang, C. Zhang, W. Li, Q. Guo, H. Gao, Y. You, Y. Li, Z. Cui, K.-C. Jiang, H. Long, D. Zhang and S. Xin, *ACS Appl. Mater. Interfaces*, 2018, **10**, 5543–5550.

4 X. Fu, P. Zamani, J.-Y. Choi, F. M. Hassan, G. Jiang, D. C. Higgins, Y. Zhang, M. A. Hoque and Z. Chen, *Adv. Mater.*, 2017, **29**, 1604456.

5 S. Liang, R. Chen, P. Yu, M. Ni, Q. Zhang, X. Zhang and W. Yang, *Chem. Commun.*, 2017, **53**, 11453–11456.

6 W. Zhang, X. Xu, C. Zhang, Z. Yu, Y. Zhou, Y. Tang, P. Wu and S. Guo, *Small Methods*, 2017, **1**, 1700167.

7 D.-H. Kwak, S.-B. Han, Y.-W. Lee, H.-S. Park, I.-A. Choi, M.-C. Kim, S.-J. Kim, D.-H. Kim, J.-I. Sohn and K.-W. Park, *Appl. Catal., B*, 2017, **203**, 889–898.

8 M. Huynh, T. Ozel, C. Liu, E. C. Lau and D. G. Nocera, *Chem. Sci.*, 2017, **8**, 4779–4794.

9 A. Bharti and G. Cheruvally, *J. Power Sources*, 2017, **360**, 196–205.

10 Y. J. Sa, D.-J. Seo, J. Woo, J. T. Lim, J. Y. Cheon, S. Y. Yang, J. M. Lee, D. Kang, T. J. Shin, H. S. Shin, H. Y. Jeong, C. S. Kim, M. G. Kim, T.-Y. Kim and S. H. Joo, *J. Am. Chem. Soc.*, 2016, **138**, 15046–15056.

11 M. Xiao, J. Zhu, L. Ma, Z. Jin, J. Ge, X. Deng, Y. Hou, Q. He, J. Li, Q. Jia, S. Mukerjee, R. Yang, Z. Jiang, D. Su, C. Liu and W. Xing, *ACS Catal.*, 2018, **8**, 2824–2832.

12 C. Yuanjun, J. Shufang, W. Yanggang, D. Juncai, C. Wenxing, L. Zhi, S. Rongan, Z. Lirong, Z. Zhongbin, W. Dingsheng and L. Yadong, *Angew. Chem.*, 2017, **56**, 6937–6941.

13 H. Zhang, S. Hwang, M. Wang, Z. Feng, S. Karakalos, L. Luo, Z. Qiao, X. Xie, C. Wang, D. Su, Y. Shao and G. Wu, *J. Am. Chem. Soc.*, 2017, **139**, 14143–14149.

14 L. Qiheng, C. Wenxing, X. Hai, G. Yue, L. Zhi, Z. Lirong, Z. Xusheng, Y. Wensheng, C. Weng-Chon, S. Rongan, F. Ninghua, G. Lin, Z. Zhongbin, C. Chen, W. Dingsheng, P. Qing, L. Jun and L. Yadong, *Adv. Mater.*, 2018, **30**, 1800588.

15 J. Wang, Z. Huang, W. Liu, C. Chang, H. Tang, Z. Li, W. Chen, C. Jia, T. Yao, S. Wei, Y. Wu and Y. Li, *J. Am. Chem. Soc.*, 2017, **139**, 17281–17284.

16 S. Kim and H. Kim, *Catal. Today*, 2017, **295**, 119–124.

17 Y. Chen, S. Ji, S. Zhao, W. Chen, J. Dong, W.-C. Cheong, R. Shen, X. Wen, L. Zheng, A. I. Rykov, S. Cai, H. Tang, Z. Zhuang, C. Chen, Q. Peng, D. Wang and Y. Li, *Nat. Commun.*, 2018, **9**, 5422.

18 W.-J. Jiang, L. Gu, L. Li, Y. Zhang, X. Zhang, L.-J. Zhang, J.-Q. Wang, J.-S. Hu, Z. Wei and L.-J. Wan, *J. Am. Chem. Soc.*, 2016, **138**, 3570–3578.

19 A. Zitolo, V. Goellner, V. Armel, M.-T. Sougrati, T. Mineva, L. Stievano, E. Fonda and F. Jaouen, *Nat. Mater.*, 2015, **14**, 937.

20 J. Li, S. Ghoshal, W. Liang, M.-T. Sougrati, F. Jaouen, B. Halevi, S. McKinney, G. McCool, C. Ma, X. Yuan, Z.-F. Ma, S. Mukerjee and Q. Jia, *Energy Environ. Sci.*, 2016, **9**, 2418–2432.

21 K. Strickland, E. Miner, Q. Jia, U. Tylus, N. Ramaswamy, W. Liang, M.-T. Sougrati, F. Jaouen and S. Mukerjee, *Nat. Commun.*, 2015, **6**, 7343.

22 Y. Wu, S. Zhao, K. Zhao, T. Tu, J. Zheng, J. Chen, H. Zhou, D. Chen and S. Li, *J. Power Sources*, 2016, **311**, 137–143.

23 J. Yang, X. Wang, B. Li, L. Ma, L. Shi, Y. Xiong and H. Xu, *Adv. Funct. Mater.*, 2017, **27**, 1606497.

24 J. Li, F. Yu, M. Wang, Y. Lai, H. Wang, X. Lei and J. Fang, *Int. J. Hydrogen Energy*, 2017, **42**, 2996–3005.

25 H. Peng, Z. Mo, S. Liao, H. Liang, L. Yang, F. Luo, H. Song, Y. Zhong and B. Zhang, *Sci. Rep.*, 2013, **3**, 1765.

26 Z. Zhang, X. Gao, M. Dou, J. Ji and F. Wang, *J. Mater. Chem. A*, 2017, **5**, 1526–1532.

27 Y.-T. Xu, X. Xiao, Z.-M. Ye, S. Zhao, R. Shen, C.-T. He, J.-P. Zhang, Y. Li and X.-M. Chen, *J. Am. Chem. Soc.*, 2017, **139**, 5285–5288.

28 B. Y. Guan, L. Yu and X. W. Lou, *Energy Environ. Sci.*, 2016, **9**, 3092–3096.

29 H. Zhang, H. Osgood, X. Xie, Y. Shao and G. Wu, *Nano Energy*, 2017, **31**, 331–350.

30 K. Shen, X. Chen, J. Chen and Y. Li, *ACS Catal.*, 2016, **6**, 5887–5903.

31 X. X. Wang, D. A. Cullen, Y.-T. Pan, S. Hwang, M. Wang, Z. Feng, J. Wang, M. H. Engelhard, H. Zhang, Y. He, Y. Shao, D. Su, K. L. More, J. S. Spendelow and G. Wu, *Adv. Mater.*, 2018, **30**, 1706758.

32 L. Jiao, G. Wan, R. Zhang, H. Zhou, S.-H. Yu and H.-L. Jiang, *Angew. Chem.*, 2018, **130**, 8661–8665.

33 X. Song, L. Guo, X. Liao, J. Liu, J. Sun and X. Li, *Small*, 2017, **13**, 1700238.

34 L. Shang, H. Yu, X. Huang, T. Bian, R. Shi, Y. Zhao, G. I. N. Waterhouse, L.-Z. Wu, C.-H. Tung and T. Zhang, *Adv. Mater.*, 2016, **28**, 1668–1674.

35 J. Tang, R. R. Salunkhe, J. Liu, N. L. Torad, M. Imura, S. Furukawa and Y. Yamauchi, *J. Am. Chem. Soc.*, 2015, **137**, 1572–1580.

36 L. Zhang, Z. Su, F. Jiang, L. Yang, J. Qian, Y. Zhou, W. Li and M. Hong, *Nanoscale*, 2014, **6**, 6590–6602.

37 M. Hu, Y. Ju, K. Liang, T. Suma, J. Cui and F. Caruso, *Adv. Funct. Mater.*, 2016, **26**, 5827–5834.

38 X. Li, Y. Feng, M. Li, W. Li, H. Wei and D. Song, *Adv. Funct. Mater.*, 2015, **25**, 6858–6866.

39 L.-S. Zhang, W. Li, Z.-M. Cui and W.-G. Song, *J. Phys. Chem. C*, 2009, **113**, 20594–20598.

40 J. Z. Y. Tan, N. M. Nursam, F. Xia, M.-A. Sani, W. Li, X. Wang and R. A. Caruso, *ACS Appl. Mater. Interfaces*, 2017, **9**, 4540–4547.

41 M. Ou, S. Wan, Q. Zhong, S. Zhang and Y. Wang, *Int. J. Hydrogen Energy*, 2017, **42**, 27043–27054.

42 Q. Jia, N. Ramaswamy, H. Hafiz, U. Tylus, K. Strickland, G. Wu, B. Barbiellini, A. Bansil, E. F. Holby, P. Zelenay and S. Mukerjee, *ACS Nano*, 2015, **9**, 12496–12505.

43 H. Peng, S. Hou, D. Dang, B. Zhang, F. Liu, R. Zheng, F. Luo, H. Song, P. Huang and S. Liao, *Appl. Catal., B*, 2014, **158**, 60–69.

44 R. Zheng, S. Liao, S. Hou, X. Qiao, G. Wang, L. Liu, T. Shu and L. Du, *J. Mater. Chem. A*, 2016, **4**, 7859–7868.

45 M.-Q. Wang, W.-H. Yang, H.-H. Wang, C. Chen, Z.-Y. Zhou and S.-G. Sun, *ACS Catal.*, 2014, **4**, 3928–3936.

46 P. Chen, T. Zhou, L. Xing, K. Xu, Y. Tong, H. Xie, L. Zhang, W. Yan, W. Chu, C. Wu and Y. Xie, *Angew. Chem., Int. Ed.*, 2016, **56**, 610–614.

47 H. Zhang, S. Hwang, M. Wang, Z. Feng, S. Karakalos, L. Luo, Z. Qiao, X. Xie, C. Wang, D. Su, Y. Shao and G. Wu, *J. Am. Chem. Soc.*, 2017, **139**, 14143–14149.

48 F. Pan, J. Jin, X. Fu, Q. Liu and J. Zhang, *ACS Appl. Mater. Interfaces*, 2013, **5**, 11108–11114.

49 D. Li, Y. Jia, G. Chang, J. Chen, H. Liu, J. Wang, Y. Hu, Y. Xia, D. Yang and X. Yao, *Chem*, 2018, **4**, 2345–2356.

50 W. Li, L.-S. Zhang, Q. Wang, Y. Yu, Z. Chen, C.-Y. Cao and W.-G. Song, *J. Mater. Chem.*, 2012, **22**, 15342–15347.

51 Y. Deng, Y. Dong, G. Wang, K. Sun, X. Shi, L. Zheng, X. Li and S. Liao, *ACS Appl. Mater. Interfaces*, 2017, **9**, 9699–9709.

52 M. Thomas, R. Illathvalappil, S. Kurungot, B. N. Nair, A. A. P. Mohamed, G. M. Anilkumar, T. Yamaguchi and U. S. Hareesh, *ACS Appl. Mater. Interfaces*, 2016, **8**, 29373–29382.

53 J. Liang, R. F. Zhou, X. M. Chen, Y. H. Tang and S. Z. Qiao, *Adv. Mater.*, 2014, **26**, 6074–6079.

54 I. Kone, A. Xie, Y. Tang, Y. Chen, J. Liu, Y. Chen, Y. Sun, X. Yang and P. Wan, *ACS Appl. Mater. Interfaces*, 2017, **9**, 20963–20973.

55 K. A. Stoerzinger, M. Risch, B. Han and Y. Shao-Horn, *ACS Catal.*, 2015, **5**, 6021–6031.

56 Y.-C. Wang, Y.-J. Lai, L. Song, Z.-Y. Zhou, J.-G. Liu, Q. Wang, X.-D. Yang, C. Chen, W. Shi, Y.-P. Zheng, M. Rauf and S.-G. Sun, *Angew. Chem.*, 2015, **127**, 10045–10048.

57 Q. Liu, X. Liu, L. Zheng and J. Shui, *Angew. Chem.*, 2018, **130**, 1218–1222.

58 L. Yang, D. Cheng, H. Xu, X. Zeng, X. Wan, J. Shui, Z. Xiang and D. Cao, *Proc. Natl. Acad. Sci. U. S. A.*, 2018, **115**, 6626–6631.

59 M. Busch, N. B. Halck, U. I. Kramm, S. Siahrostami, P. Krtil and J. Rossmeisl, *Nano Energy*, 2016, **29**, 126–135.

60 Q. Jia, N. Ramaswamy, U. Tylus, K. Strickland, J. Li, A. Serov, K. Artyushkova, P. Atanassov, J. Anibal, C. Gumeci, S. C. Barton, M.-T. Sougrati, F. Jaouen, B. Halevi and S. Mukerjee, *Nano Energy*, 2016, **29**, 65–82.

61 U. I. Kramm, J. Herranz, N. Larouche, T. M. Arruda, M. Lefevre, F. Jaouen, P. Bogdanoff, S. Fiechter, I. Abs-Wurmbach, S. Mukerjee and J.-P. Dodelet, *Phys. Chem. Chem. Phys.*, 2012, **14**, 11673–11688.

62 U. I. Kramm, M. Lefèvre, N. Larouche, D. Schmeisser and J.-P. Dodelet, *J. Am. Chem. Soc.*, 2014, **136**, 978–985.

63 A. Zitolo, V. Goellner, V. Armel, M.-T. Sougrati, T. Mineva, L. Stievano, E. Fonda and F. Jaouen, *Nat. Mater.*, 2015, **14**, 937–942.

64 S. Liang, R. Chen, P. Yu, M. Ni, Q. Zhang, X. Zhang and W. Yang, *Chem. Commun.*, 2017, **53**, 11453–11456.

65 E. F. Holby and C. D. Taylor, *Sci. Rep.*, 2015, **5**, 9286.

66 S. Hou, B. Chi, G. Liu, J. Ren, H. Song and S. Liao, *Electrochim. Acta*, 2017, **253**, 142–150.